Experimental Evaluation of Structural Intensity in Two-Dimensional Plate-Type Locally Resonant Elastic Metamaterials

H. Al Ba'ba'a
Mechanical and Aerospace Engineering Department, University at Buffalo (SUNY), Buffalo, NY 14260

M. A. Attarzadeh
Mechanical and Aerospace Engineering Department, University at Buffalo (SUNY), Buffalo, NY 14260

M. Nouh[1]
Mechanical and Aerospace Engineering Department, University at Buffalo (SUNY), Buffalo, NY 14260
e-mail: mnouh@buffalo.edu

Elastic metamaterials utilize locally resonant mechanical elements to onset band gap characteristics that are typically exploited in vibration suppression and isolation applications. The present work employs a comprehensive structural intensity analysis (SIA) to depict the structural power distribution and variations associated with band gap frequency ranges, as well as outside them along both dimensions of a two-dimensional (2D) metamaterial. Following a brief theoretical dispersion analysis, the actual mechanics of a finite metamaterial plate undergoing flexural loading and consisting of a square array of 100 cells is examined experimentally using a fabricated prototype. Scanning laser Doppler vibrometer (SLDV) tests are carried out to experimentally measure the deformations of the metamaterial in response to base excitations within a broad frequency range. In addition to confirming the attenuation and blocked propagation of elastic waves throughout the elastic medium via graphical visualizations of power flow maps, the SIA reveals interesting observations, which give additional insights into energy flow and transmission in elastic metamaterials as a result of the local resonance effects. A drastic reduction in power flow magnitudes to the bulk regions of the plate within a band gap is noticeably met with a large amplification of structural intensity around and in the neighborhood of the excitation source as a compensatory effect. Finally, the theoretical and experimentally measured streamlines of power flow are presented as an alternative tool to predict the structural power patterns and track vortices as well as confined regions of energy concentrations. [DOI: 10.1115/1.4039042]

Keywords: metamaterials, local resonance, power flow, structural intensity

1 Introduction

Elastic metamaterials are a class of subwavelength structures that house an array of locally resonating subcomponents, which contribute to the rise of intriguing mechanical and elastodynamic characteristics such as a negative effective mass and mechanically tunable frequency band gaps [1–4]. The interplay between the host structure and counter inertial forces in the internal resonators has been shown to onset unique vibration absorption capabilities over extended frequency ranges in addition to enhanced damping properties in dissipative realizations of such systems [5]. As a result, they have recently become widely appealing for a wide range of vibroacoustic mitigation applications. Over the past decade, considerable effort has been devoted to studying different types of locally resonant metamaterials including, but not limited to, elastic bars [6], flexural beams [7,8], torsional structures [9], as well as two-dimensional (2D) membranes and plates [10–12]. Since the bulk macroscopic of elastic metamaterials predominantly rely on the local resonance effects, a large body of work has also recently focused on active and controllable elastic metamaterials via piezoelectric shunting [13], electric actuation [14], and for energy harvesting applications [15].

Elastic metamaterials typically consist of a self-repeated unit cell that contains a base structure and one or more internal mechanical resonators. Owing to their periodic configuration, wave propagation and dispersion characteristics are often predicted using a simplified analysis of an individual cell. The commonly adopted mathematical techniques include the Bloch-wave solution and the transfer matrix method [16,17]. However, by definition, wave dispersion and band gap characteristics obtained from such methods predict the behavior of infinitely long realizations of the unit cell [18]. As a result, the response of actual metamaterials often deviates from the theoretical unit cell-based models, motivating deeper investigations into the behavior of finite metamaterials [19–21]. Among these is the use of structural intensity as a tool to track and quantify mechanical power flow, as opposed to elastic wave propagation, associated with such structures within and outside band gap ranges. A comprehensive mathematical framework for structural intensity analysis (SIA) has been derived for plain, stepped, and stiffened plates [22–24], plates with welded connections and varying thickness [25,26], and in damage detection and health monitoring of laminated composite plates [27,28]. More recently, the SIA has been applied in the context of locally resonant elastic metamaterials and shown to be a robust approach in evaluating the existence of, or absence thereof, a band gap [29]. Further, the SIA has been also utilized to predict the influence of material and viscoelastic damping on the emerging band gaps in phononic (periodic) structures for different damping amounts rendering it a valuable tool in the performance prediction of dissipative metamaterials [30].

In this work, we extend the developed SIA approach to 2D metamaterial systems (namely locally resonant plate-type structures) and, furthermore, provide a detailed account of the experimental measurements of the different structural intensity representations. In addition to comparing the experimentally measured power flow patterns with the mathematical output, the mechanical energy amplitude is utilized to locate the metamaterial plate's band gap frequency ranges, which are validated against the dispersion curve predictions. The experimental SIA evaluation is carried out using scanning laser Doppler vibrometry (SLDV) measurements of the metamaterial's response to base excitations imposed by an electrodynamic shaker. Postprocessing of the displacement fields is then carried out to obtain the mechanical

[1]Corresponding author.

Contributed by the Applied Mechanics Division of ASME for publication in the Journal of Applied Mechanics. Manuscript received November 8, 2017; final manuscript received January 11, 2018; published online February 2, 2018. Assoc. Editor: Yihui Zhang.

power flow and energy streamline maps. This paper is organized in four sections. Following the introduction, the elastic and geometric parameters of the metamaterial prototype are outlined followed by a mathematical overview of both the dispersion and the structural intensity analysis and governing equations. Next, the different results from the experimental and numerical investigations are presented followed by a brief summary and conclusions.

2 The Metamaterial Plate

The metamaterial plate considered comprises locally resonant unit cells, which consist of a square metallic ring that is connected to an internal plate via a thin elastic beam (neck). The configuration used is a single-material design that is inspired from literature [31]. The combination of the neck and the connected plate provides the internal spring-mass type system needed to onset the local resonance effects culminating in the band gap characteristics. The plate consists of 100 cells of 24 mm × 24 mm size as shown in Fig. 1. The plate specimen is machined from a solid plate of aluminum alloy with a total length of 270 mm, a width of 243 mm and a thickness $t = 2.54$ mm with an elastic modulus and density of 70 GPa and 2700 kg/m^3, respectively. The internal mass is a 15 mm × 15 mm plate suspended by a 3 mm wide beam. The motion of interest in this study is the out-of-plane transverse (bending) deflection. As such, the analysis is based on the Kirchhoff–Love theory for thin plates that captures the deflections depending on the transverse deformation w and its derivatives in space, i.e., θ_x and θ_y.

2.1 Unit Cell Dispersion Analysis. The dispersion relations of the metamaterial plate are developed based on the finite element method, which is discussed here in brief [32]. The unit cell is discretized into square four-node elements of a 1.5 mm × 1.5 mm. After appropriately deriving the mass and stiffness matrices of the unit cell, the dynamics of the unit cell is described as

$$\mathbf{M}_c\ddot{\mathbf{x}} + \mathbf{K}_c\mathbf{x} = 0 \tag{1}$$

where $\mathbf{M}_c$ and $\mathbf{K}_c$ are the cell mass and stiffness matrices, respectively. The element stiffness and mass matrices are obtained via a displacement shape function from which the strain equations can be generated. Once the strain matrix is derived, the elasticity matrix $\mathbf{E}$ is used to obtain the potential energy, and consequently the element stiffness matrix

$$\mathbf{K}_e = \frac{t^3}{12}\mathbf{A}^{-T}\int_{-a}^{a}\int_{-a}^{a}\mathbf{L}_\mathbf{K}^T\mathbf{E}\mathbf{L}_\mathbf{K}\mathrm{d}x\mathrm{d}y\mathbf{A}^{-1} \tag{2}$$

where $\mathbf{L}_\mathbf{K}$ and $\mathbf{A}$ are the shape function's second derivative matrix and the shape function's evaluations at the element nodes. Similarly, from the kinetic energy, the element mass matrix can be obtained as

$$\mathbf{M}_e = \varrho\mathbf{A}^{-T}\int_{-a}^{a}\int_{-a}^{a}\mathbf{L}_\mathbf{M}^T\mathbf{H}\mathbf{L}_\mathbf{M}\mathrm{d}x\mathrm{d}y\mathbf{A}^{-1} \tag{3}$$

where ϱ is the material density and $\mathbf{L}_\mathbf{M}$ is a matrix of the utilized shape function and its first derivatives while

$$\mathbf{H} = \mathbf{diag}\begin{bmatrix} t & \frac{t^3}{12} & \frac{t^3}{12}\end{bmatrix} \tag{4}$$

A more detailed description of computing $\mathbf{K}_e$ and $\mathbf{M}_e$ can be found in Refs. [8] and [12]. The matrices $\mathbf{M}_c$ and $\mathbf{K}_c$ are reduced by applying the Bloch–Floquet boundary conditions that require the degrees-of-freedom, given by the nodal deflection vector $\mathbf{x}$, to be divided into nine groups as shown in Fig. 2(*a*) such that

$$\mathbf{x} = \{\mathbf{x}_\mathrm{i}\ \mathbf{x}_\mathrm{B}\ \mathbf{x}_\mathrm{T}\ \mathbf{x}_\mathrm{L}\ \mathbf{x}_\mathrm{R}\ \mathbf{x}_\mathrm{LB}\ \mathbf{x}_\mathrm{RB}\ \mathbf{x}_\mathrm{LT}\ \mathbf{x}_\mathrm{RT}\}^\mathrm{T} \tag{5}$$

where the subscripts i, B, T, L, and R denote internal, bottom, top, left, and right nodes, respectively. As such, the transformation $\mathbf{x} = \boldsymbol{Q}\hat{\boldsymbol{x}}$ can be applied for a harmonic analysis such that

$$[\hat{\mathbf{K}}_c - \omega^2\hat{\mathbf{M}}_c]\hat{\mathbf{x}} = 0 \tag{6}$$

where $\hat{\mathbf{x}} = \{\mathbf{x}_\mathrm{i}\ \mathbf{x}_\mathrm{B}\ \mathbf{x}_\mathrm{L}\ \mathbf{x}_\mathrm{LB}\}^\mathrm{T}$, $\hat{\mathbf{K}}_c = \bar{\mathbf{Q}}^\mathrm{T}\mathbf{K}_\mathbf{c}\mathbf{Q}$, $\hat{\mathbf{M}}_c = \bar{\mathbf{Q}}^\mathrm{T}\mathbf{M}_\mathbf{c}\mathbf{Q}$, and $\mathbf{Q}$ is a transformation matrix, which can be expressed as

$$\mathbf{Q} = \begin{bmatrix} \mathbf{I} & 0 & 0 & 0 \\ 0 & \mathbf{I} & 0 & 0 \\ 0 & \mathbf{I}e^{i\mu_y} & 0 & 0 \\ 0 & 0 & \mathbf{I} & 0 \\ 0 & 0 & \mathbf{I}e^{i\mu_x} & 0 \\ 0 & 0 & 0 & \mathbf{I} \\ 0 & 0 & 0 & \mathbf{I}e^{i\mu_x} \\ 0 & 0 & 0 & \mathbf{I}e^{i\mu_x} \\ 0 & 0 & 0 & \mathbf{I}e^{i(\mu_x+\mu_y)} \end{bmatrix} \tag{7}$$

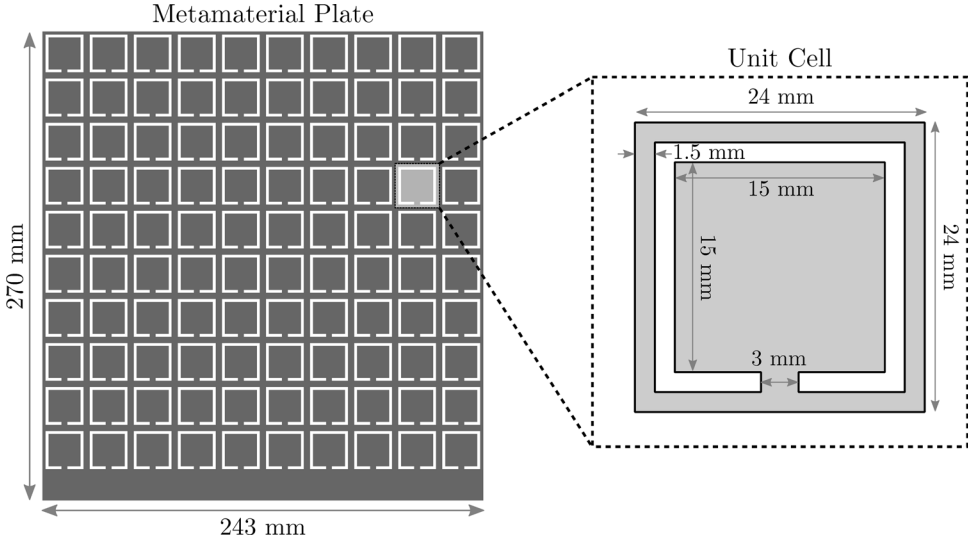

Fig. 1 Schematic of the metamaterial plate and its unit cell along with their dimensions

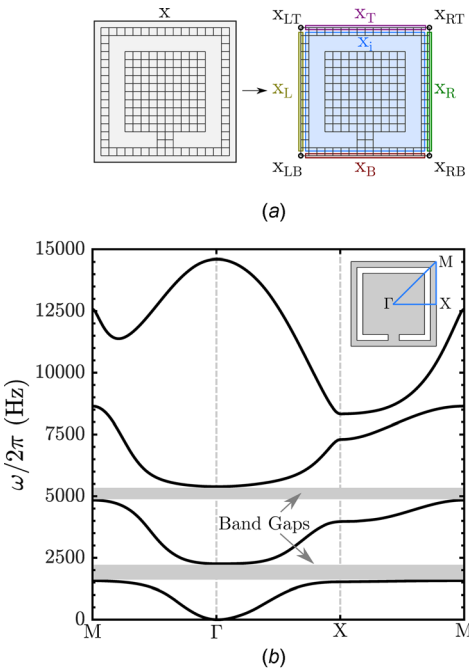

Fig. 2 (*a*) Discretization of the unit cell and the arrangement of the degrees-of-freedom groups and (*b*) the dispersion curves for the unit cell shown in Fig. 1

where μ_x and μ_y are the wavenumbers (spatial frequencies) in the x and y directions, $\mathbf{I}$ is the identity matrix, $i = \sqrt{-1}$, and $\bar{\mathbf{Q}}^{\mathrm{T}}$ is the Hermitian transpose of the matrix $\mathbf{Q}$. The dispersion relations can then be attained by sweeping the values of the wavenumbers μ_x and μ_y across the irreducible Brillouin zone and by solving the eigenvalue problem in Eq. (6) for the angular frequency ω. Figure 2(*b*) shows the dispersion curves for the unit cell under consideration where the first band gap spans the frequency range $1569 < \omega/2\pi < 2259$ Hz, which is the one of interest in this study.

While Fig. 2(*b*) represents the dispersion characteristics as predicted by the Kirchhoff-plate theory, such results can be verified using a complete three-dimensional (3D) model that comprises solid elements. The latter would account for both in-plane and out-of-plane motions as well as any thickness effects of the plate. Figure 3 shows the dispersion curves generated for the same metamaterial plate using the 3D model as well as how it compares to the Kirchhoff theory predictions. The figure also discriminates between out-of-plane and in-plane modes at several points on different dispersion branches, for which the corresponding deformation modes are given. It can be seen that the Kirchhoff theory shows a strong agreement with the 3D model for all the transverse modes. In addition to being less computationally intensive, this also confirms that the Kirchhoff model is reliable and sufficiently accurate to carry out the numerical analysis for this particular plate.

2.2 Structural Intensity Analysis. Structural intensity is defined as the vibrational power per unit cross-sectional area flowing in a structure undergoing dynamic loading. The general formula to obtain the instantaneous structural intensity is given by [33]

$$i_k(t) = -\sigma_{kj}(t)v_j(t) \tag{8}$$

where $i_k(t)$ is the kth component of the instantaneous structural intensity in the time domain, $\sigma_{kj}(t)$ is the stress tensor at a point where k is the normal direction of the area, and $v_j(t)$ is the velocity vector in the j-direction, where $k = 1, 2, 3$ and $j = 1, 2, 3$. For a Kirchhoff plate undergoing transverse motion, the instantaneous structural intensity in the x and y directions can be hence reduced to [23]

$$I_x(t) = -[\dot{w}(t)Q_x(t) + \dot{\theta}_y(t)M_x(t) - \dot{\theta}_x M_{xy}(t)] \tag{9a}$$

$$I_y(t) = -[\dot{w}(t)Q_y(t) - \dot{\theta}_x(t)M_y(t) + \dot{\theta}_y M_{yx}(t)] \tag{9b}$$

In Eqs. (9*a*) and (9*b*), w is the transverse deflection of the plate, $\theta_x = \partial w/\partial y$ is the bending angle in the x-direction, $\theta_y = -\partial w/\partial x$ is the bending angle in the y-direction, while $\dot{(\cdot)}$ denotes the derivative in time. $Q_x(t)$ and $Q_y(t)$ are the shear forces in the x and y directions, respectively, and $M_x(t)$, $M_y(t)$, $M_{xy}(t)$ and $M_{yx}(t)$ are the internal moments. In the frequency domain, the steady-state structural intensity $I_k(\omega)$ can be computed via a Fourier transform of Eq. (8), which yields [34]

$$I_k(\omega) = -\frac{1}{2}\sigma_{kj}(\omega)v_j^*(\omega) = P(\omega) + iQ(\omega) \tag{10}$$

where $\sigma_{kj}(\omega)$ is the frequency-dependent stress tensor and $v_j^*(\omega)$ is the complex conjugate of the frequency-dependent velocity. The complex structural intensity $I_k(\omega)$ can be decomposed into

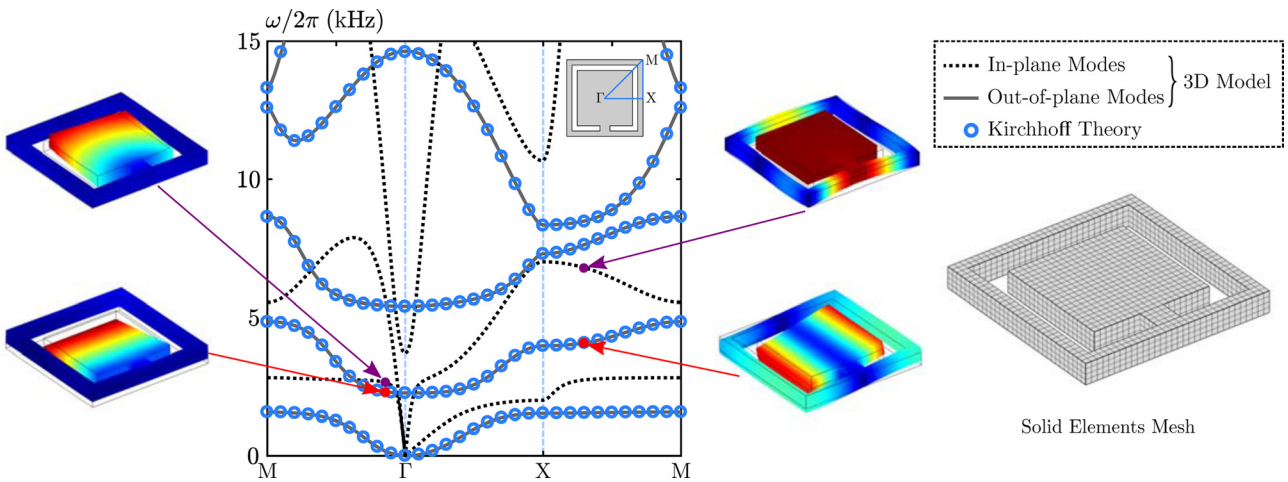

Fig. 3 In-plane (dashed) and out-of-plane (solid) dispersion curves (and corresponding deformation modes) for the shown unit cell mesh obtained via a 3D model of solid elements. Kirchhoff predictions (circles) are shown for comparison.

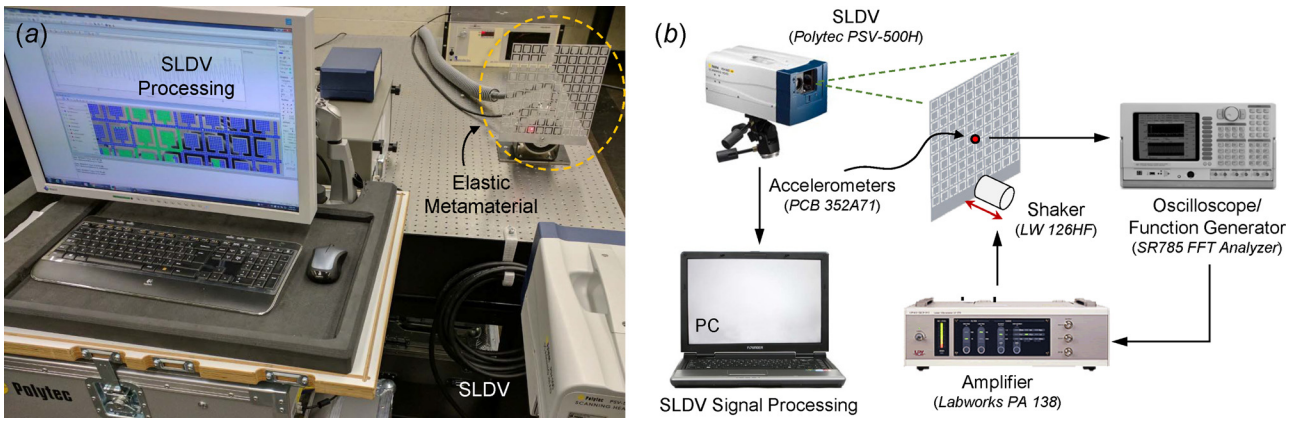

Fig. 4 (*a*) The experimental setup consisting of the vibrometer, the magnifier, the electrodynamic shaker and the metamaterial plate and (*b*) a flow diagram of the experimental testing

imaginary and real terms to obtain the active $P(\omega)$ and reactive $Q(\omega)$ power components, respectively. Similar to Eqs. (9*a*) and (9*b*), the steady-state active power flow along the x- and y-directions of the Kirchhoff plate can be expressed as

$$P_x(\omega) = -\frac{1}{2}\omega \mathbf{Im}\left[Q_x(\omega)w^*(\omega) + M_x(\omega)\theta_y^*(\omega) - M_{xy}(\omega)\theta_x^*(\omega)\right] \tag{11a}$$

$$P_y(\omega) = -\frac{1}{2}\omega \mathbf{Im}\left[Q_y(\omega)w^*(\omega) - M_y(\omega)\theta_x^*(\omega) + M_{yx}(\omega)\theta_y^*(\omega)\right] \tag{11b}$$

3 Experimental Analysis and Results

3.1 Experimental Setup. The experimental study is performed using the setup shown in Fig. 4(*a*). In the experimental tests, a machined prototype of the elastic metamaterial plate (shown in Fig. 1) is anchored to an electrodynamic shaker and excited at its base using a signal fed from a function generator through an amplifier. The metamaterial's vibrational response is measured using a 100 kHz polytec SLDV. The SLDV is synchronized with the excitation signal fed to the shaker and its head shines a laser beam that scans the plate's vibrating surface enabling it to measure surface deformations and velocities using time of travel calculations. Displacement measurements at approximately 13,000 points, evenly distributed along the plate's surface, constitute the experimental displacement field. Such measurement resolution, while time costly, ensures that the flexural wave propagation is accurately captured. The schematic diagram shown in Fig. 4(*b*) illustrates the various components of the experimental setup.

3.2 Frequency Response of the Metamaterial Plate. To verify the presence of the theoretically predicted band gap in Sec. 2.1, the frequency response function of the finite plate is measured via a sine sweep of a broad frequency spectrum that includes the band gap range. The frequency response is displayed for an arbitrary point at the midspan of the plate, as highlighted in Fig. 5(*a*), via a discrete sensor. The experimentally measured frequency response is shown in Fig. 5(*b*) and is compared to its numerical counterpart from the finite element description of the plate. The dispersion-predicted ($1569 < \omega/2\pi < 2259$ Hz) and measured ($1550 < \omega/2\pi < 2275$ Hz) band gap frequency ranges are found to be in reasonable agreement. The discrepancies between the numerical and experimental frequency responses can be understandably attributed to (1) machining imperfections and tolerances in the physical metamaterial prototype resulting in small variations of thickness and resonators dimensions along both the x- and y-directions and (2) structural and viscous damping differences, which typically influence the attenuation magnitude within the theoretically predicted band gaps.

3.3 Displacement Field. Both the theoretical analysis and the experimentally obtained frequency responses identify a band gap in the elastic metamaterial in the approximate range between

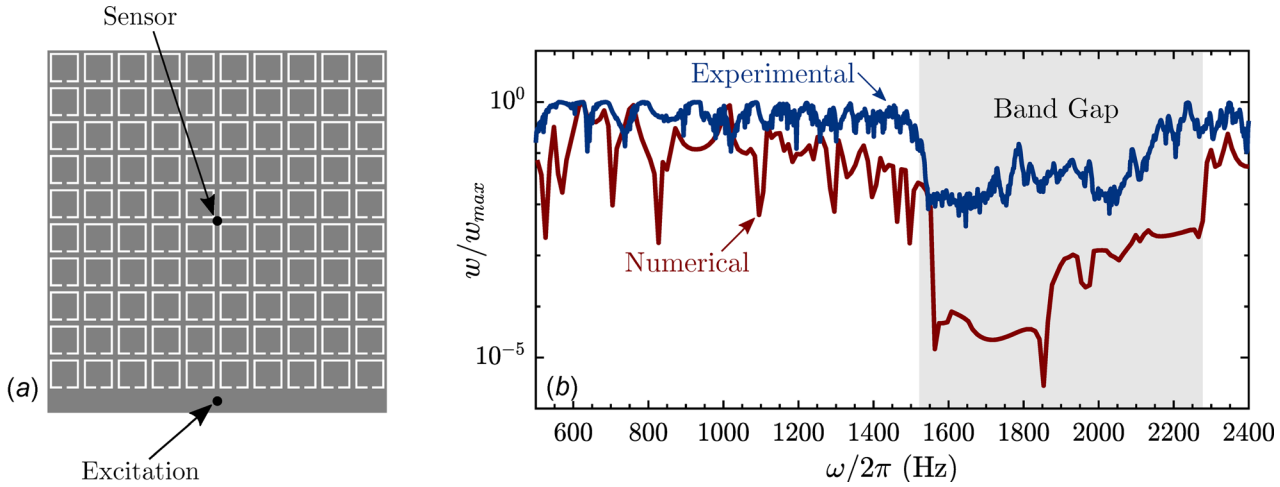

Fig. 5 (*a*) Schematic diagram illustrating the sensing and excitation locations on the metamaterial plate and (*b*) the numerical and experimental frequency response function at the sensing location

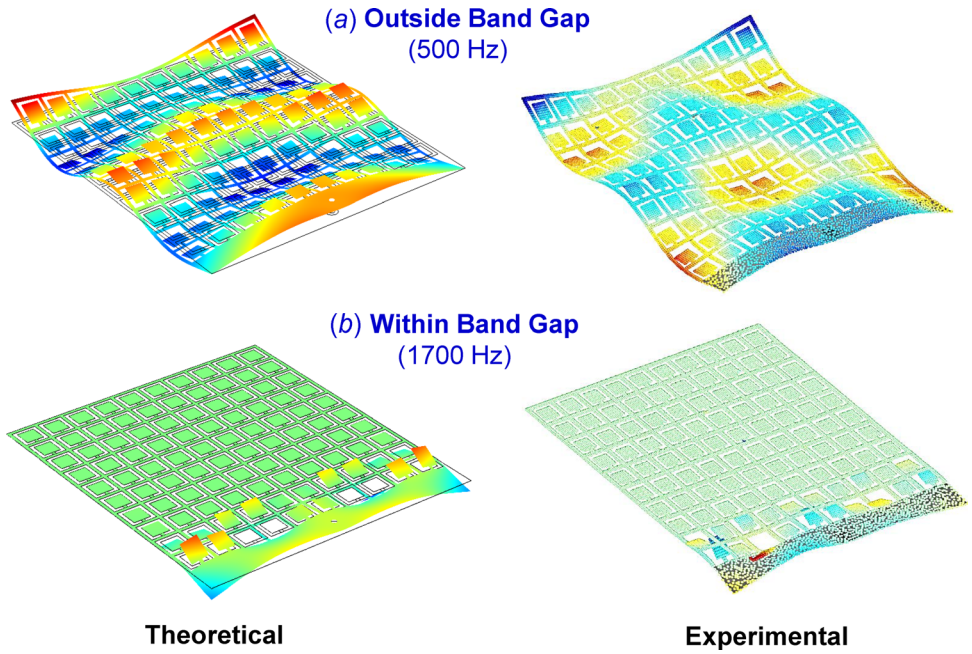

Fig. 6 Numerical and experimental displacement fields at a (*a*) pass band frequency (500 Hz) and (*b*) a band gap frequency (1700 Hz)

1550 and 2275 Hz. To experimentally visualize this, we select 500 Hz as a representative frequency outside the band gap (i.e., a pass band frequency) and 1700 Hz for a frequency within the band gap range. The displacement fields of the metamaterial plate at the two frequencies are obtained both theoretically via a harmonic analysis of the finite element model and experimentally from the SLDV scanned measurements. Figure 6 displays both sets which graphically illustrate how the propagation of waves emerging from the shaker (excitation source) is impeded in the plate when excited inside a band gap. On the contrary, such waves propagate freely to the end of the metamaterial outside that range. It can also be observed that the source vibrations are predominantly absorbed into the first couple of local resonator rows within the band gap.

3.4 Structural Intensity Analysis and Power Flow Maps. Equations (11*a*) and (11*b*) are utilized to evaluate the structural intensity distribution corresponding to both excitation frequencies (500 and 1700 Hz). Figure 7 summarizes the numerical and experimental SIA computational procedures. The experimentally obtained structural intensity is based on the hybrid approach presented in Ref. [22], which utilizes the experimentally measured displacement field (in this case, using the SLDV) while computing

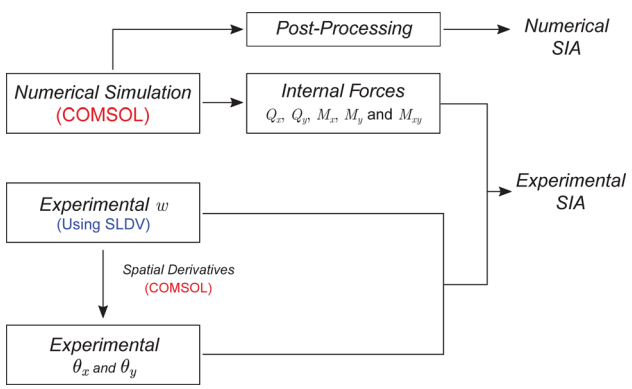

Fig. 7 Flow chart illustrating the procedure of the numerical and experimental SIA computations

the internal forces within the structure numerically. The structural mechanics module of the commercial COMSOL MULTIPHYSICS package is used here for that purpose. The experimental bending angles θ_x and θ_y are calculated from the spatial derivative of the transverse deflection matrix w obtained from the SLDV.

Figures 8 and 9 show the power flow maps obtained at 500 and 1700 Hz, respectively, for both the theoretical and experimental cases. In these figures, the power flow maps are presented as an array of arrows that emerge from the power source (excitation location) and propagate throughout the structure. The direction and the magnitude of each individual arrow depend on the values of the two active power components P_x and P_y at that respective location. Figures 8 and 9 show that the power flow patterns are alternative indicative of wave propagation trends and reveal that energy transmission in the plate is effectively blocked within a band gap. It can also be seen that, despite the apparent deformations of the second row of resonators (as shown in Fig. 6(*b*)), power flow to these cells is almost negligible, which reflects the weakness of the internal forces at these nodes. More importantly, by comparing the active power magnitudes at the base of the metamaterial plate and in the vicinity of the excitation source, much larger energy concentrations can be observed within a band gap frequency than outside it, a feature that is not necessarily evident in the deformation shapes. The amplified structural intensity closer to the source is indicative of the entrapped power as a result of the strong counter inertial forces in the local resonances. This interchange between strong vibration attenuation and magnified power closer to the source within a metamaterial can be exploited to enhance energy harvesting and extraction capabilities of such structures as attempted, for e.g., in Ref. [15].

The frequency response of the active power magnitude $|P|$ (where $|P| = \sqrt{P_x^2 + P_y^2}$) gives an additional insight into how the blocked power flow to the bulk area of the metamaterial plate within a band gap is simultaneously met with a noticeable increase in the power intensity in the small area in the neighborhood of the exciting source. Figures 10 and 11 show the evolution of $|P|$ as the excitation frequency increases for a point close to the source and the sensor point (marked earlier on Fig. 5(*a*)), respectively. Both figures are augmented with close-ups of the power flow maps surrounding both points. The gradual increase in the

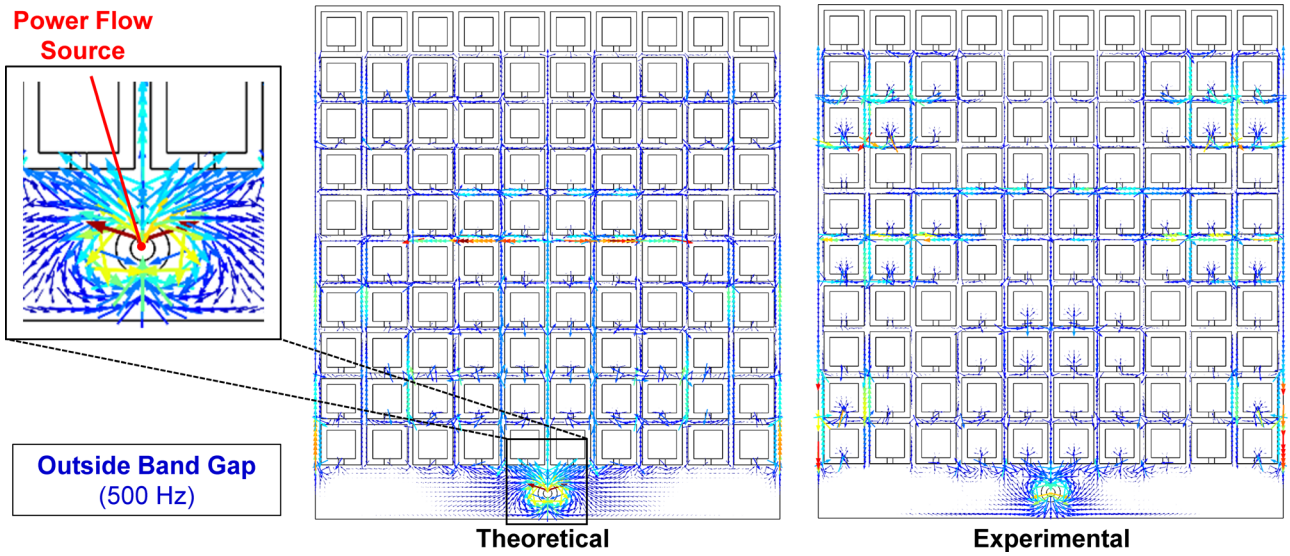

Fig. 8 Theoretical and experimental power flow maps for the pass band frequency (500 Hz)

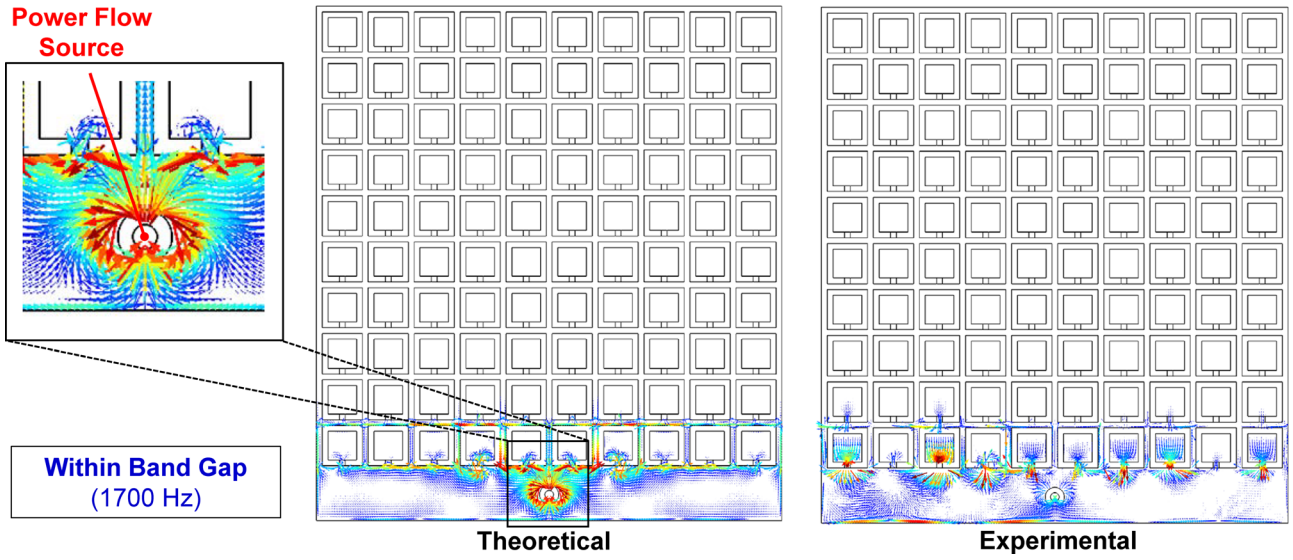

Fig. 9 Theoretical and experimental power flow maps for the band gap frequency (1700 Hz)

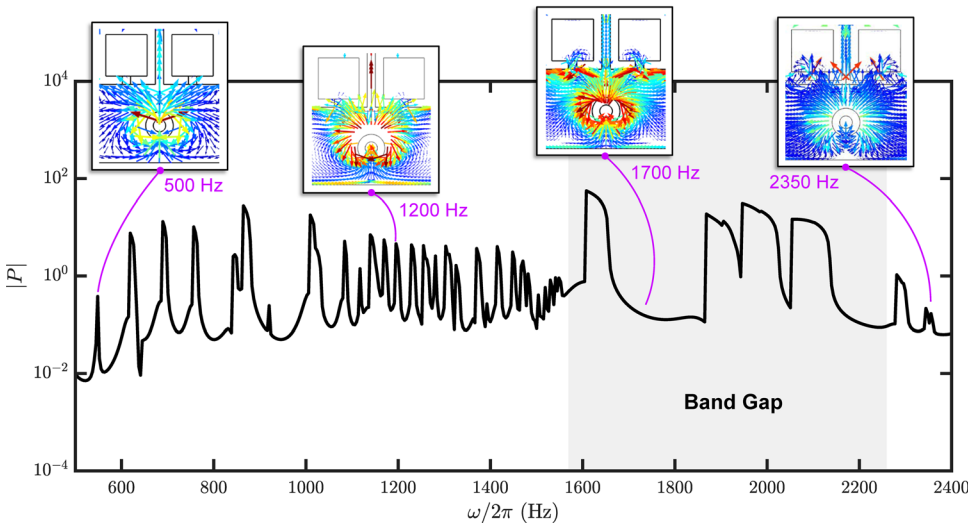

Fig. 10 The frequency response of the active power magnitude $|P|$ function at a point near the excitation source and select close-ups of the power flow map in its neighborhood

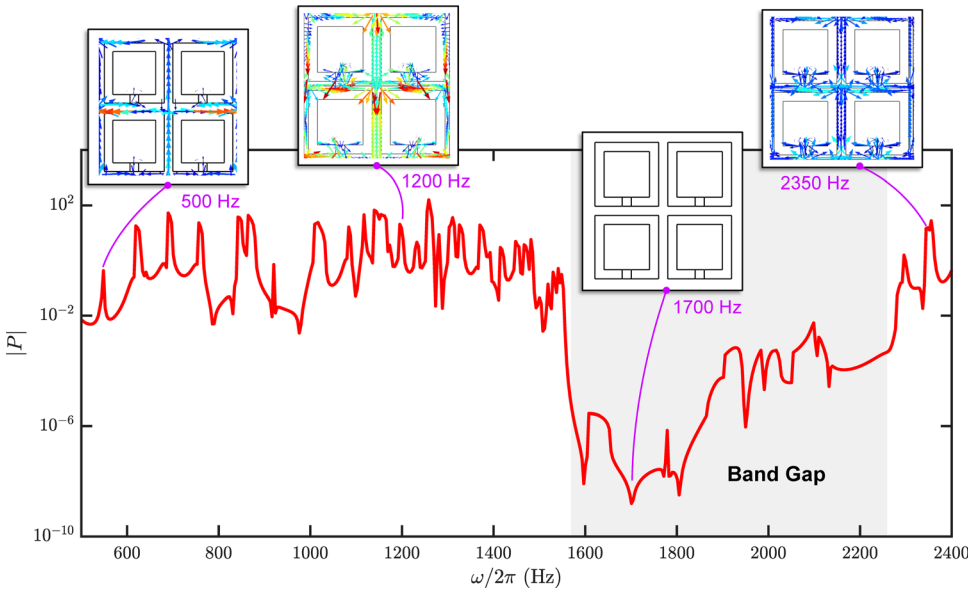

Fig. 11 The frequency response of the active power magnitude $|P|$ function at the sensing point and select close-ups of the power flow map in its neighborhood

power intensity near the source can be clearly seen in Fig. 10 up until the band gap range (shaded area), after which the magnitudes of the arrows go back to normal levels. The opposite trend exactly takes place in Fig. 11 where there is completely no power flow at and around the sensing point within the band gap range while there is noticeable power flow before and after it. The increase in power flow near the source during a band gap can be also intuitively understood in the context of overall energy conservation at any given band gap frequency. Such increase compensates for the local resonance band gap effect, which effectively hinders energy transmission to the plate boundaries resulting in magnified energy sinks at the vicinity of the source as a direct consequence.

3.5 Streamline Representations. The streamline representation is an interesting alternative technique to quantify structural power flow patterns in mechanically loaded elastic metamaterials. The streamlines provide a visualization, which describes the velocity field as a gradient of a scalar function. Such representations are capable of revealing additional underlying mechanics of energy transport within an elastic structure such as vortex-like patterns. In addition, they can reflect the speed of the power transmission in the structure which is proportional to the relative spacing between the flow streamlines. Structural power flow streamlines are mathematically obtained via a cross product of the energy flow particle position $d\mathbf{r}$ and the structural intensity vectors [35] and can be expressed as

$$d\mathbf{r} \times \mathbf{I}(\mathbf{r}, t) = 0 \tag{12}$$

which, for a steady-state harmonic response in a 2D structure, reduces to

$$\frac{dx}{P_x} = \frac{dy}{P_y} \tag{13}$$

Figures 12 and 13 show the streamline representations obtained at 500 and 1700 Hz, respectively, for both the theoretical and experimental cases. Similar to the power flow maps, the streamlines are nonexistent in the bulk part of the metamaterial plate when excited at a band gap frequency. In addition to the high

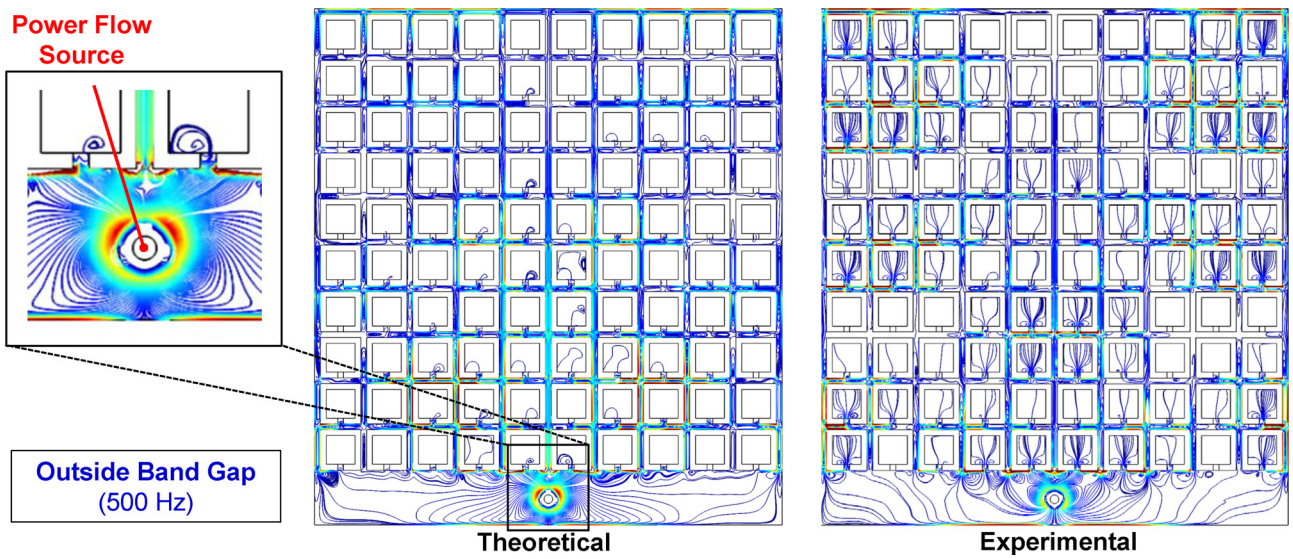

Fig. 12 Theoretical and experimental streamlines of power flow for the pass band frequency (500 Hz)

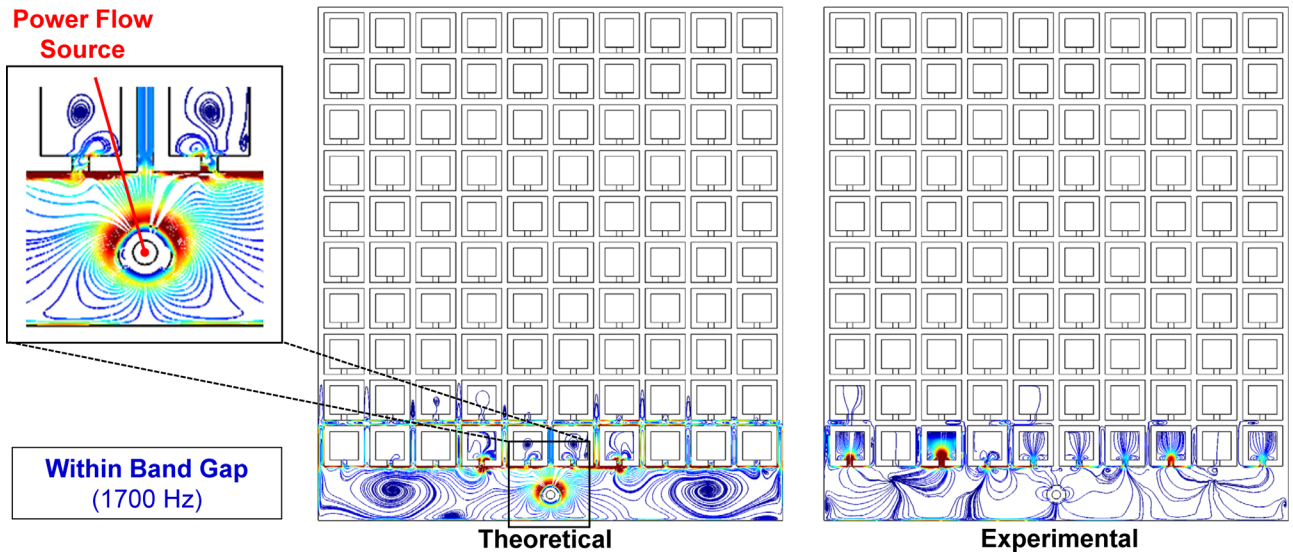

Fig. 13 Theoretical and experimental streamlines of power flow for the band gap frequency (1700 Hz)

magnitudes at the base of the plate corresponding to a band gap frequency, it can also be observed that the intensity streamlines have a much heavier presence into the resonators closer to the excitation source inside a band gap as compared to outside it. As a result of the impeded energy transmission, the structural intensity is entrapped in vortices, which span almost the entire space of the resonators in the vicinity of the exciting source. It can also be seen that the resonators closest to the excitation source all comprise hot spots at the resonator necks as well as the anchors connecting them to the base structure. In addition to being regions of high stress concentrations, these can also be interpreted in light of the resonator design. If the locally resonant component is to be thought of as a discrete spring-mass mechanism, the resonator neck and its supporting edges would serve as the inner spring where the largest deformations take place within a band gap. Additionally, the experimental portion of Fig. 13 shows a couple of hot spots on two of the first row resonators closer to the left end of the plate. By referring to the experimentally measured displacement fields (Fig. 6), it can be seen that the resonator deformations are not perfectly symmetric about the center (in contrast to their numerical counterparts) with particularly large deformations in the neighborhood of the same aforementioned resonators. Such discrepancies are typical due to both machining imperfections and resultant variations of both the thickness and resonator dimensions. Finally, the circulating flux in the resonators is expected and common in small finite structural components with no power flow exits (outlets).

4 Conclusions

A theoretical and experimental investigation of vibrational power transmission in plate-type locally resonant elastic metamaterials has been presented. Starting from a Kirchhoff–Love model for thin plates undergoing flexural deformations, the dispersion characteristics of the self-repeating unit cell of the metamaterial plate were theoretically obtained via a finite element model. The dispersion curves were used to predict the location of the local resonance band gap. Following the dispersion analysis, the actual mechanics of a finite metamaterial plate consisting of a square array of 100 cells were examined both numerically and experimentally on a manufactured specimen. SLDV tests were carried out to experimentally measure the entire deformation field of the metamaterial at different frequencies of interest and were used to verify the band gap behavior. By utilizing energy rather than a displacement-based approach, a structural intensity analysis was employed to depict the power flow maps corresponding to band gap conditions as well as outside them. In addition to using power flow to confirm the presence of wave propagation band gaps due to local resonance effects, the magnitudes and direction of structural power flow along the different regions of the metamaterial plate revealed some interesting observations. The drastic reduction of power flow to the bulk area of the plate as a result of a band gap was found to be met with a noticeable magnification of structural intensity around and in the vicinity of the exciting source as a compensatory effect. Such confined energy traps can be a double-edged weapon. While favorable for potential energy extraction or harvesting applications, their long-term effect on the structural integrity and durability of this class of metamaterials can be detrimental. Such findings concretize the value of using the SIA as a valuable, yet overlooked, tool in the performance evaluation of finite and physically realizable elastic metamaterials.

Acknowledgment

Thanks are extended to Buffalo Manufacturing Works (operated by EWI) for their help in the manufacturing of the experimental specimen.

Funding Data

- The U.S. National Science Foundation (Grant No. CMMI 1647744).

References

[1] Huang, H. H., Sun, C. T., and Huang, G. L., 2009, "On the Negative Effective Mass Density in Acoustic Metamaterials," Int. J. Eng. Sci., **47**(4), pp. 610–617.
[2] Huang, H. H., and Sun, C. T., 2011, "A Study of Band-Gap Phenomena of Two Locally Resonant Acoustic Metamaterials," Proc. Inst. Mech. Eng., Part N, **224**(3), pp. 83–92.
[3] Baravelli, E., and Ruzzene, M., 2013, "Internally Resonating Lattices for Bandgap Generation and Low-Frequency Vibration Control," J. Sound Vib., **332**(25), pp. 6562–6579.
[4] Zhu, R., Liu, X., Hu, G., Sun, C., and Huang, G., 2014, "A Chiral Elastic Metamaterial Beam for Broadband Vibration Suppression," J. Sound Vib., **333**(10), pp. 2759–2773.
[5] Hussein, M. I., and Frazier, M. J., 2013, "Metadamping: An Emergent Phenomenon in Dissipative Metamaterials," J. Sound Vib., **332**(20), pp. 4767–4774.
[6] Pai, P. F., 2010, "Metamaterial-Based Broadband Elastic Wave Absorber," J. Intell. Mater. Syst. Struct., **21**(5), pp. 517–528.
[7] Pai, P. F., Peng, H., and Jiang, S., 2014, "Acoustic Metamaterial Beams Based on Multi-Frequency Vibration Absorbers," Int. J. Mech. Sci., **79**, pp. 195–205.
[8] Nouh, M., Aldraihem, O., and Baz, A., 2014, "Vibration Characteristics of Metamaterial Beams With Periodic Local Resonances," ASME J. Vib. Acoust., **136**(6), p. 61012.

[9] Bigoni, D., Guenneau, S., Movchan, A. B., and Brun, M., 2013, "Elastic Metamaterials With Inertial Locally Resonant Structures: Application to Lensing and Localization," Phys. Rev. B, **87**(17), p. 174303.
[10] Krushynska, A., Kouznetsova, V., and Geers, M., 2014, "Towards Optimal Design of Locally Resonant Acoustic Metamaterials," J. Mech. Phys. Solids, **71**, pp. 179–196.
[11] Peng, H., and Pai, P. F., 2014, "Acoustic Metamaterial Plates for Elastic Wave Absorption and Structural Vibration Suppression," Int. J. Mech. Sci., **89**, pp. 350–361.
[12] Nouh, M., Aldraihem, O., and Baz, A., 2015, "Wave Propagation in Metamaterial Plates With Periodic Local Resonances," J. Sound Vib., **341**, pp. 53–73.
[13] Chen, Y., Huang, G., and Sun, C., 2014, "Band Gap Control in an Active Elastic Metamaterial With Negative Capacitance Piezoelectric Shunting," ASME J. Vib. Acoust., **136**(6), p. 061008.
[14] Nouh, M., Aldraihem, O., and Baz, A., 2016, "Periodic Metamaterial Plates With Smart Tunable Local Resonators," J. Intell. Mater. Syst. Struct., **27**(13), pp. 1829–1845.
[15] Gonella, S., To, A. C., and Liu, W. K., 2009, "Interplay Between Phononic Bandgaps and Piezoelectric Microstructures for Energy Harvesting," J. Mech. Phys. Solids, **57**(3), pp. 621–633.
[16] Mead, D., 1970, "Free Wave Propagation in Periodically Supported, Infinite Beams," J. Sound Vib., **11**(2), pp. 181–197.
[17] Bloch, F., 1929, "Über die Quantenmechanik der Elektronen in Kristallgittern," Z. Phys., **52**(7–8), pp. 555–600.
[18] Hussein, M. I., Leamy, M. J., and Ruzzene, M., 2014, "Dynamics of Phononic Materials and Structures: Historical Origins, Recent Progress, and Future Outlook," ASME Appl. Mech. Rev., **66**(4), p. 040802.
[19] Hvatov, A., and Sorokin, S., 2015, "Free Vibrations of Finite Periodic Structures in Pass- and Stop-Bands of the Counterpart Infinite Waveguides," J. Sound Vib., **347**, pp. 200–217.
[20] Sugino, C., Leadenham, S., Ruzzene, M., and Erturk, A., 2016, "On the Mechanism of Bandgap Formation in Locally Resonant Finite Elastic Metamaterials," J. Appl. Phys., **120**(13), p. 134501.
[21] Al Ba'ba'a, H., Nouh, M., and Singh, T., 2017, "Formation of Local Resonance Band Gaps in Finite Acoustic Metamaterials: A Closed-Form Transfer Function Model," J. Sound Vib., **410**, pp. 429–446.
[22] Petrone, G., De Vendittis, M., De Rosa, S., and Franco, F., 2016, "Numerical and Experimental Investigations on Structural Intensity in Plates," Compos. Struct., **140**, pp. 94–105.
[23] Cho, D.-S., Choi, T.-M., Kim, J.-H., and Vladimir, N., 2016, "Structural Intensity Analysis of Stepped Thickness Rectangular Plates Utilizing the Finite Element Method," Thin-Walled Struct., **109**, pp. 1–12.
[24] Tadina, M., Ragnarsson, P., Pluymers, B., Donders, S., Desmet, W., and Boltezar, M., 2008, "On the Use of an FE Based Energy Flow Post-Processing Method for Vehicle Structural Dynamic Analysis," International Conference on Noise and Vibration Engineering (ISMA), Leuven, Belgium, Sept. 15–17, pp. 1609–1620.
[25] Cieślik, J., and Bochniak, W., 2014, "Vibration Energy Flow in Welded Connection of Plates," Arch. Acoust., **31**(4), pp. 53–58.
[26] Cieślik, J., 2004, "Vibration Energy Flow in Rectangular Plates," J. Theor. Appl. Mech., **42**(1), pp. 195–212.
[27] Semperlotti, F., and Conlon, S. C., 2010, "Structural Damage Identification in Plates Via Nonlinear Structural Intensity Maps," J. Acoust. Soc. Am., **127**(2), pp. EL48–EL53.
[28] Lamberti, A., and Semperlotti, F., 2013, "Detecting Closing Delaminations in Laminated Composite Plates Using Nonlinear Structural Intensity and Time Reversal Mirrors," Smart Mater. Struct., **22**(12), p. 125006.
[29] Al Ba'ba'a, H., and Nouh, M., 2017, "Mechanics of Longitudinal and Flexural Locally Resonant Elastic Metamaterials Using a Structural Power Flow Approach," Int. J. Mech. Sci., **122**, pp. 341–354.
[30] Al Ba'ba'a, H., and Nouh, M., 2017, "An Investigation of Vibrational Power Flow in One-Dimensional Dissipative Phononic Structures," ASME J. Vib. Acoust., **139**(2), p. 021003.
[31] Wang, Y.-F., and Wang, Y.-S., 2013, "Complete Bandgap in Three-Dimensional Holey Phononic Crystals With Resonators," ASME J. Vib. Acoust., **135**(4), p. 041009.
[32] Veres, I. A., Berer, T., and Matsuda, O., 2013, "Complex Band Structures of Two Dimensional Phononic Crystals: Analysis by the Finite Element Method," J. Appl. Phys., **114**(8), p. 083519.
[33] Gavrić, L., and Pavić, G., 1993, "A Finite Element Method for Computation of Structural Intensity by the Normal Mode Approach," J. Sound Vib., **164**(1), pp. 29–43.
[34] Li, Y., and Lai, J., 2000, "Prediction of Surface Mobility of a Finite Plate With Uniform Force Excitation by Structural Intensity," Appl. Acoust., **60**(3), pp. 371–383.
[35] Xu, X., Lee, H. P., Lu, C., and Guo, J. Y., 2005, "Streamline Representation for Structural Intensity Fields," J. Sound Vib., **280**(1–2), pp. 449–454.